











Cite this: *Chem. Sci.*, 2025, 16, 4831

All publication charges for this article have been paid for by the Royal Society of Chemistry

Exceeding flexexpectations: a combined experimental and computational investigation of structural flexibility in 3-dimensional linker-based metal–organic frameworks†

Courtney S. Smoljan, ^a Filip Formalik, ^{ab} Michael L. Barsoum, ^{‡c} Kira M. Fahy, ^{‡d} Madeleine A. Gaidimas, ^{‡d} Florencia A. Son, ^{‡d} Haomiao Xie, ^d Karam B. Idrees, ^d Omar K. Farha ^{*ad} and Randall Q. Snurr ^{*a}

Designing sorbents for the separation of molecules with sub-angstrom differences in size requires precise control over pore size and environment, which can be challenging to establish in the presence of structural flexibility. However, metal–organic frameworks (MOFs) that incorporate 3-dimensional (3D) linkers—ditopic ligands with 3-dimensional, sterically bulky cores—are well-suited to address this challenge, as 3D linkers enable sub-angstrom level control over pore size by mitigating the effects of structural flexibility. In this study, we used a combined computational and experimental approach to quantify flexibility in two systems of MOFs with increasing linker bulkiness, leveraging these systems to distinguish between two classes of flexibility: global and local. Specifically, we used density functional theory (DFT) calculations to understand the electronic energy landscapes of MIL-53(Al), MIL-47(V) and their corresponding 3D linker analogues of increasing bulkiness. We further characterized the mechanical properties of these materials with DFT calculations of elastic tensors and in practical compression conditions using *in situ* variable pressure X-ray diffraction experiments. Finally, we illustrated the importance of establishing sub-angstrom level pore control by demonstrating the effects of each type of flexibility on the adsorption properties of MOFs using grand canonical Monte Carlo simulations.

Received 20th September 2024

Accepted 31st January 2025

DOI: 10.1039/d4sc06360k

rsc.li/chemical-science

Introduction

Metal–organic frameworks (MOFs) are crystalline, nanoporous materials that have been investigated for a wide variety of applications including heterogeneous catalysis, gas storage, and chemical separations.^{1–4} Their construction *via* the coordination of metal ions or clusters and organic linkers generates a seemingly infinite library of structures that can be tuned toward a desired application.⁵ Within this diverse class of structures, many MOFs exhibit flexible behavior, such as linker rotation, breathing, swelling, or sub-net sliding, which can

introduce interesting properties and potential applications for these materials.⁶ However, when designing MOFs for the separation of molecules with sub-angstrom differences in size, including hexane or xylene isomers and olefin/paraffin mixtures, it is critical to establish precise control over a MOF's pore size and environment,^{7,8} which can be challenging when these types of flexibility are in play.⁹

To establish this precise control, our groups and others previously demonstrated that increasing linker dimensionality in MOFs is an effective strategy.^{10–16} In most cases, MOFs are built from 2-dimensional (2D) linkers, *i.e.*, ditopic ligands that are distinguished by their planar and aromatic cores.¹⁷ However, the inherent planarity of these linkers leaves many of the resulting MOF structures subject to structural flexibility. In the case of linker orientation, the rotation of 2D linkers in the pore structure of a MOF can result in important changes in pore size, even though the other atoms in the structure remain relatively fixed.^{18,19} These changes can significantly affect the adsorptive properties of MOFs.²⁰ In contrast, installing 3-dimensional (3D) linkers, *i.e.* ditopic ligands with bulky cores that exhibit 3-fold symmetry or higher, minimizes the impact of linker rotation on the pore environment. While 3D linkers are still subject to rotation in the structure,²¹ these linkers mitigate

^aDepartment of Chemical and Biological Engineering, Northwestern University, Evanston, IL 60208, USA. E-mail: o-farha@northwestern.edu; snurr@northwestern.edu

^bDepartment of Micro, Nano, and Bioprocess Engineering, Faculty of Chemistry, Wrocław University of Science and Technology, Wrocław 50-370, Poland

^cDepartment of Materials Science and Engineering, Northwestern University, Evanston, IL 60208, USA

^dDepartment of Chemistry and International Institute for Nanotechnology, Northwestern University, Evanston, IL 60208, USA

† Electronic supplementary information (ESI) available. CCDC 2347333. For ESI and crystallographic data in CIF or other electronic format see DOI: <https://doi.org/10.1039/d4sc06360k>

‡ These authors contributed equally.

variations in pore size because their bulky cores evenly protrude into the pore, independent of their orientation.^{17,22} Further, many 2D linker-based MOFs exhibit phase transitions that can greatly affect the MOF's pore structure. These phase transitions are characterized by switching between two or more metastable states, which is typically instigated by an external stimulus, like temperature, pressure, or guest adsorption.^{6,23} Because 2D linkers lack steric bulk, phase transitions can be common in these materials, often resulting in switching between “closed pore” and “open pore” phases; however, 3D linkers provide steric hindrance that can stabilize open pores when these transitions occur¹⁰ or prevent phase transitions altogether.^{11,12} Through these mechanisms, incorporating 3D linkers in MOFs reduces structural flexibility, stabilizing pore environments for effective molecular sieving of molecules with similar sizes.^{17,22}

Our groups successfully applied this strategy of increasing linker dimensionality in the MIL-53 system.^{11–13} MIL-53 is a MOF that has been studied extensively due to its breathing behavior, which results in a large volume change of approximately 40% between its narrow pore (np) and large pore (lp) phases.^{23–26} MIL-53 comprises 1-dimensional channels, formed by the coordination of metal-hydroxo chains with 2D 1,4-benzenedicarboxylate (BDC) linkers. These channels crystallize in the *sra* topology, forming a “wine-rack” type structure. This structure can be synthesized from a variety of metal cations including aluminum, chromium, and scandium, among others. MIL-47 is an analogous structure containing vanadium cations that are thought to be bridged by -oxo groups, rather than -hydroxo groups as in MIL-53.²⁷ In our previous work, we installed 3D linkers of increasing bulkiness (bicyclo[1.1.1]pentane-1,3-dicarboxylate (BPDCA),¹¹ bicyclo[2.2.2]octane-1,4-dicarboxylate (BODCA)¹³ and *p*-carborane-1,12-dicarboxylate (*pC*)¹²) in MIL-53(Al) and MIL-47(V) to evaluate their effects on minimizing structural breathing and separating mixtures of hexane or xylene isomers.

In this work, we use density functional theory (DFT) and compression experiments to describe the mechanical properties of in these two systems of MOFs, exhibiting increasing linker bulkiness. Understanding the mechanical stability of these frameworks is important for assessing their suitability for industrial separations. However, directly comparing the stability of 2D linker-based MOFs with 3D linker-based MOFs is not necessarily straightforward, due to phase transitions that more commonly occur in 2D linker systems. Because of this, there is a need to distinguish between types of flexibility in these materials in order to appropriately compare values of mechanical stability. To address this, we classify structural flexibility into two categories: local flexibility and global flexibility. These terms differentiate between the types of energetics that drive flexibility in MOFs and other porous materials. We illustrate this concept in the context of energy-volume relationships in the aforementioned families of MOFs.

Specifically, we describe local flexibility as distortions at a local energy minimum. These distortions can result from small shifts in volume, such as in normal and negative thermal expansion or in elastic compression (Fig. 1a). Global flexibility describes phase transitions that significantly affect the size or

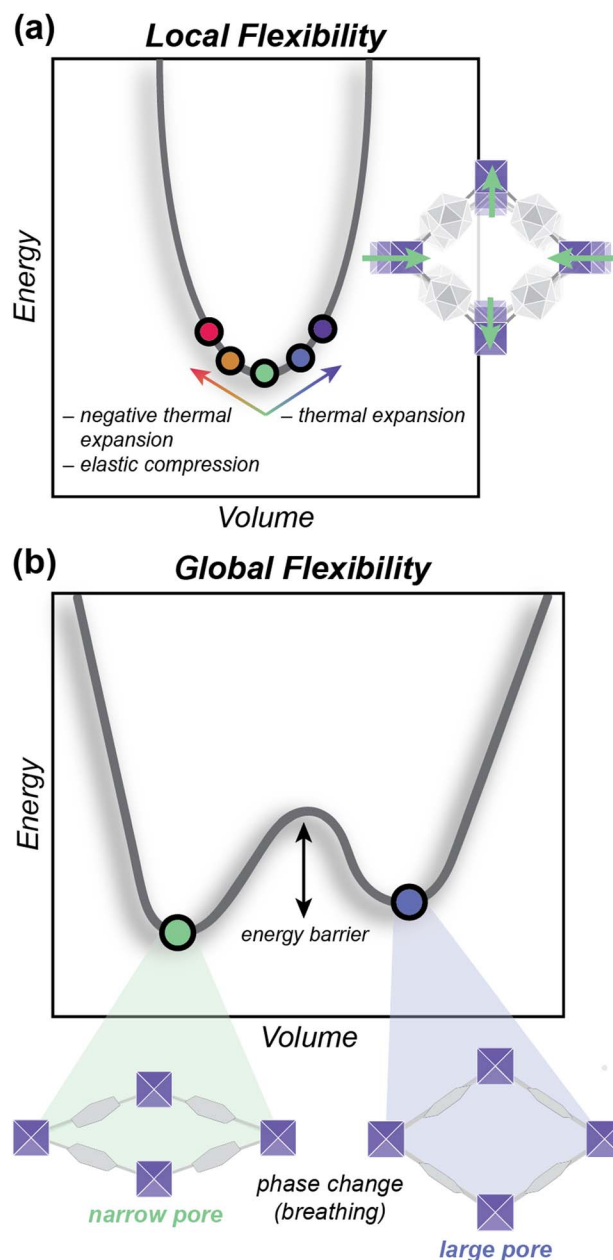


Fig. 1 Schematic representation of flexibility types in MOFs. (a) Local flexibility describes distortions near a local minimum on the energy/volume landscape. These distortions can manifest in small shifts in volume (such as in normal and negative thermal expansion or in elastic compression) or in changes in the orientations of local features like linkers or capping groups on a MOF node. The colored points represent different positions in the energy well that can be accessed through changes in temperature and pressure. (b) Global flexibility describes switching between multiple possible states (energy minima on an energy/volume landscape) driven by external stimuli like temperature, pressure, or guest adsorption.

shape of the entire unit cell, rather than only one component in the unit cell (ex. linker orientation). These phase transitions result from switching between two or more energy minima on an energy landscape (Fig. 1b).²² In our systems, we characterized global and local flexibility through the lens of energy-volume



diagrams and elastic tensors, respectively, and used these results to calculate each MOF's mechanical properties (Young's moduli and bulk moduli). Because these mechanical properties are derived from each material's local behavior, we propose using these metrics as quantitative indicators of local flexibility. To understand the behavior of 3D linker-based MOFs in practical conditions, we performed compression experiments in combination with X-ray diffraction. Finally, we demonstrated the impact that each type of flexibility can have on adsorption processes through simulated argon adsorption using grand canonical Monte Carlo (GCMC).

Our combined computational and experimental approach provides a framework to fully characterize the origin (local or global) and extent of flexibility in each MOF structure, demonstrating the necessity of these classifications of flexibility. Additionally, our findings further emphasize the importance of increasing linker dimensionality on sub-angstrom level control of a MOF's pore. We hope that this analysis of structural flexibility and mechanical properties will prompt the community to consider the driving force of flexibility in other porous systems from the perspective of energetics and leverage these definitions when comparing the flexibility and mechanical stability in porous materials.

Results and discussion

Distinguishing types of flexibility using energy–volume diagrams

To understand if breathing or other phase changes are possible in 3D linker-based MOFs, we generated energy–volume diagrams from fixed volume geometry optimizations using density functional theory (DFT). See ESI Section 2.1 for details.† We validated the accuracy of our methodology by comparing our results to the energy–volume diagram for MIL-53(Al) reported by Hoffman *et al.*, as they used a similar setup in their calculations (Fig. 2c).²⁵ For the 2D linker-based structures, MIL-53(Al) and MIL-47(V), the energy–volume diagrams show two minima, corresponding with their well-studied narrow pore and large pore phases (Fig. 2). These minima correspond to volumes of 842 and 1435 Å³ for MIL-53(Al) and 899 and 1552 Å³ for MIL-47(V). In contrast, the energy–volume diagrams of the structures that incorporate the BODCA linkers (NU-2000 and NU-2001) and the pC linkers (NU-2004 and NU-2005) show a single minimum, supporting our previous observations from variable temperature powder X-ray diffraction (VT-PXRD) experiments, which demonstrated no phase changes upon heating.¹² These minima occur at 1358, 1560, 1568, and 1632 Å³ for NU-2000, NU-2001, NU-2004, and NU-2005, respectively. It should also be noted that NU-2001 retains linkers in half of its unit cells after washing and activation (Fig. S2a†),¹³ which further stabilize the open pore structure and result in a narrow energy minimum, as distorting the volume is more energetically disfavored due to the presence of these additional linkers. Although the experimental crystal structures show this linker in the pore, we also generated a hypothetical structure of NU-2001 that contains no guest molecules in the channels, referred to as NU-2001 (no guest) throughout the remainder of this manuscript (Fig. S2b†).

We generated its energy volume diagram for completeness (Fig. 2d and e). As we expected, when we manually remove the linker from the pore of NU-2001, the minimum shifts to a slightly smaller volume of 1432 Å³ and broadens.

In the cases of the structures that incorporate the BPDCA linker (NU-2002 and NU-2003), we observe global minima around 1125 and 1222 Å³, respectively, corresponding well with the experimental unit cell volumes determined from single crystal X-ray diffraction experiments (1083 and 1154 Å³, respectively).¹¹ However, we also observe local minima at smaller volumes (835 and 870 Å³, respectively), indicating the potential existence of closed pore phases in these structures. These closed pore phases are analogous to the closed pore phase of MIL-53(Sc), as they distort into a high-energy, condensed form (Fig. S9†).²⁸ While the energy–volume diagrams generated by DFT show that these closed pore phases may exist in NU-2002 and NU-2003, we do not observe them in experimental conditions, as the energy barriers required to access these phases are too high.²⁹

These results demonstrate that by installing 3-dimensional linkers in the *sra* topology, global flexibility, characterized by multiple possible phases that are accessible using external stimuli, like temperature, pressure, or guest adsorption, is mitigated or even eliminated. Next, we explore the impact of increasing linker bulkiness on local flexibility (small shifts around an energy minimum) using elastic tensors.

Exploring mechanical properties as a metric of local flexibility

Conventional metrics of mechanical stability, such as a material's bulk modulus or Young's modulus, describe the stiffness of a material in the elastic regime, *i.e.* the regime in which a material's energy–strain relationship is quadratic and, therefore, its resulting stress–strain relationship is linear. The stiffness of the material within this regime refers to the material's resistance to distortion from its energy minimum upon compression (Fig. 1a). These distortions do not switch the system from one minimum to another (breathing) as shown in Fig. 1b, but rather shift the minimum toward lower volumes (Fig. 1a). As such, values of Young's modulus or bulk modulus do not account for global flexibility (phase transitions), making their meaning convoluted for complex, dynamic systems, like many flexible MOFs. In traditional materials, high moduli values signify high mechanical stability; however, to understand the complete picture of mechanical stability in MOFs, researchers should account for other factors, like phase transitions, crystallinity, *etc.* In this section, we calculate the Young's moduli of our systems with increasing linker dimensionality. Because Young's moduli are good descriptors of elastic behavior, we use them to quantify local flexibility in 3D linker-based structures in comparison to the analogous 2D linker-based structures. Specifically, Young's modulus is a measure of a material's stiffness when subjected to unidirectional stress (Fig. S3†). We calculated the spatial dependence of Young's modulus from the elastic tensor, obtained from independent normal and shear strains, following a procedure



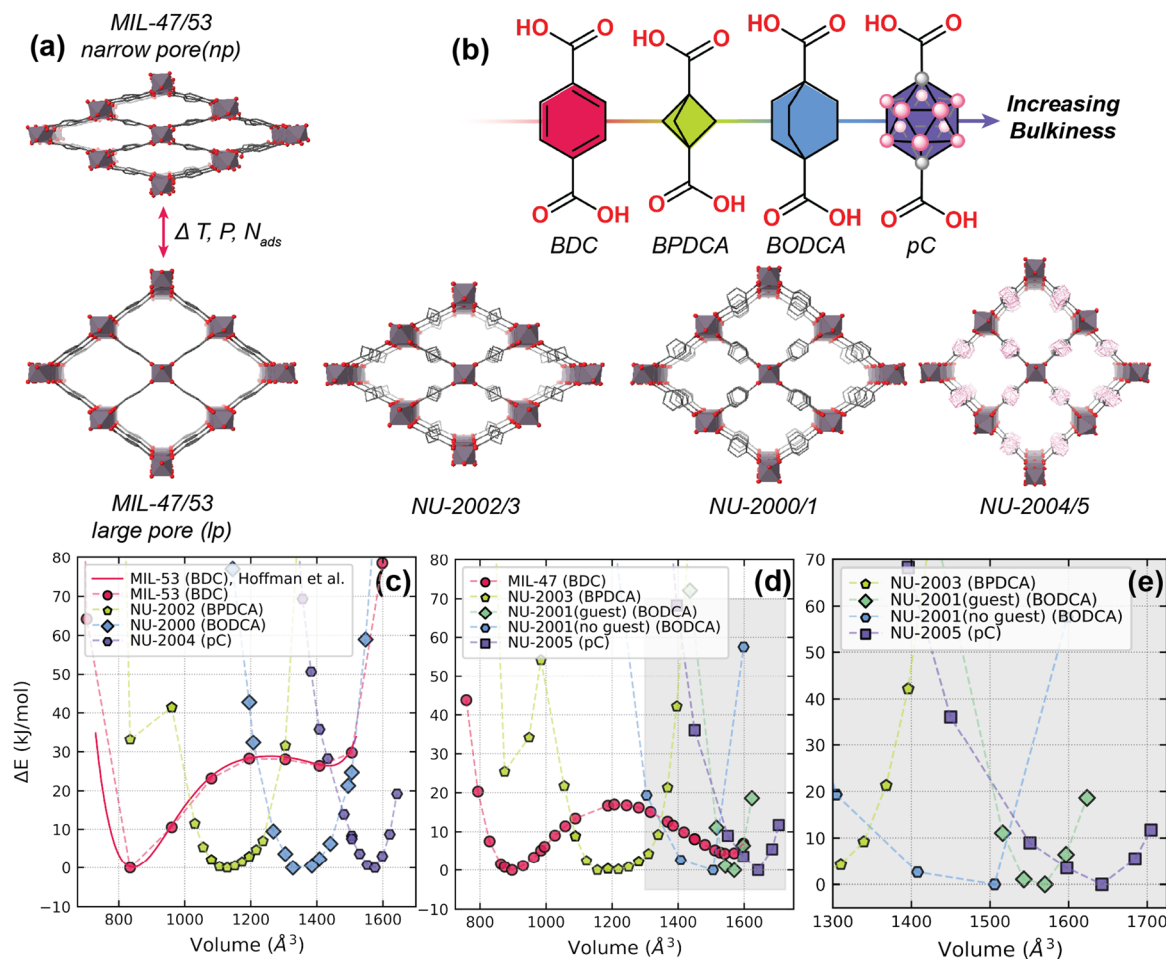


Fig. 2 (a) Representative crystal structures of MIL-53(Al)(np), MIL-53(Al)(lp), NU-2002/3, NU-2000/1, and NU-2004/5 and (b) their corresponding linker components of increasing bulkiness: 1,4-benzenedicarboxylic acid (BDC), bicyclo[1.1.1]pentane-1,3-dicarboxylic acid (BPDCA), bicyclo[2.2.2]octane-1,4-dicarboxylic acid (BODCA), and *p*-carborane-1,12-dicarboxylic acid (pC). Electronic energy–volume diagrams for (c) MIL-53(Al) and (d and e) MIL-47(V) and their corresponding 3D linker-based structural analogues generated from density functional theory geometry optimizations. Energies are reported in kJ mol^{-1} , where a mole refers to a single unit cell.

proposed by Gaillac *et al.*³⁰ For a detailed description of these calculations, see ESI Section 2.2.†

As shown in Fig. 3, in their open pore forms, MIL-53(Al) and MIL-47(V) exhibit highly anisotropic elastic behavior, with relatively high values of Young's moduli in the direction of the linkers and the inorganic chains and low values in the *y*- and *z*-directions. These relatively low values indicate that they are highly compressible in these directions. This behavior is well-known for materials comprising the compliant wine-rack motif, *i.e.* MOFs built from ditopic rigid linkers and connected by rigid pillars (nodes) to form topologies with 1-dimensional diamond shaped channels.^{31,32} In contrast, the spatial dependence of Young's moduli in the narrow pore structure of MIL-53(Al) significantly deviates from that of the open pore structure as shown in Fig. 3b. MIL-53(np) is much more difficult to compress in the *z*-direction since it is already in a highly contracted form and exhibits a Young's modulus of 75.1 GPa (Table 1). Further compression in the *y*-direction is energetically disfavored because the atoms from adjacent linker components begin to repel each other. The Young's modulus in

the *z*-direction is 5.8 GPa, which is similar to that of the large pore structure. Both the narrow pore phase and the large pore phase of MIL-53(Al) can exist at ambient conditions,²³ while pressure is required to access the narrow pore phase of MIL-47(V).³³

The structures built from 3D linkers demonstrate Young's moduli profiles with similar features to the open pore structures of MIL-47(V) and MIL-53(Al) (*i.e.*, high Young's modulus in the direction of the linker and low Young's modulus in the *y*- and *z*-directions) as shown in Fig. 3b and c. Due to these similarities (as well as the large volumes), we conclude that our 3DL-based structures are akin to the "open pore" structures of MIL-53 and MIL-47 structures and we focus the majority of our comparative analysis accordingly. Each of the 3D linker-based structures demonstrates higher values of Young's moduli in the most relevant directions of the compliant wine-rack motif (*y* and *z*) when compared to the 2D linker analogues, which is consistent with our hypothesis that installing 3D linkers can rigidify flexible frameworks (Table 1). Specifically, large pore MIL-53(Al) has a Young's modulus of 1.2 GPa in the *z*-direction, while NU-2002,



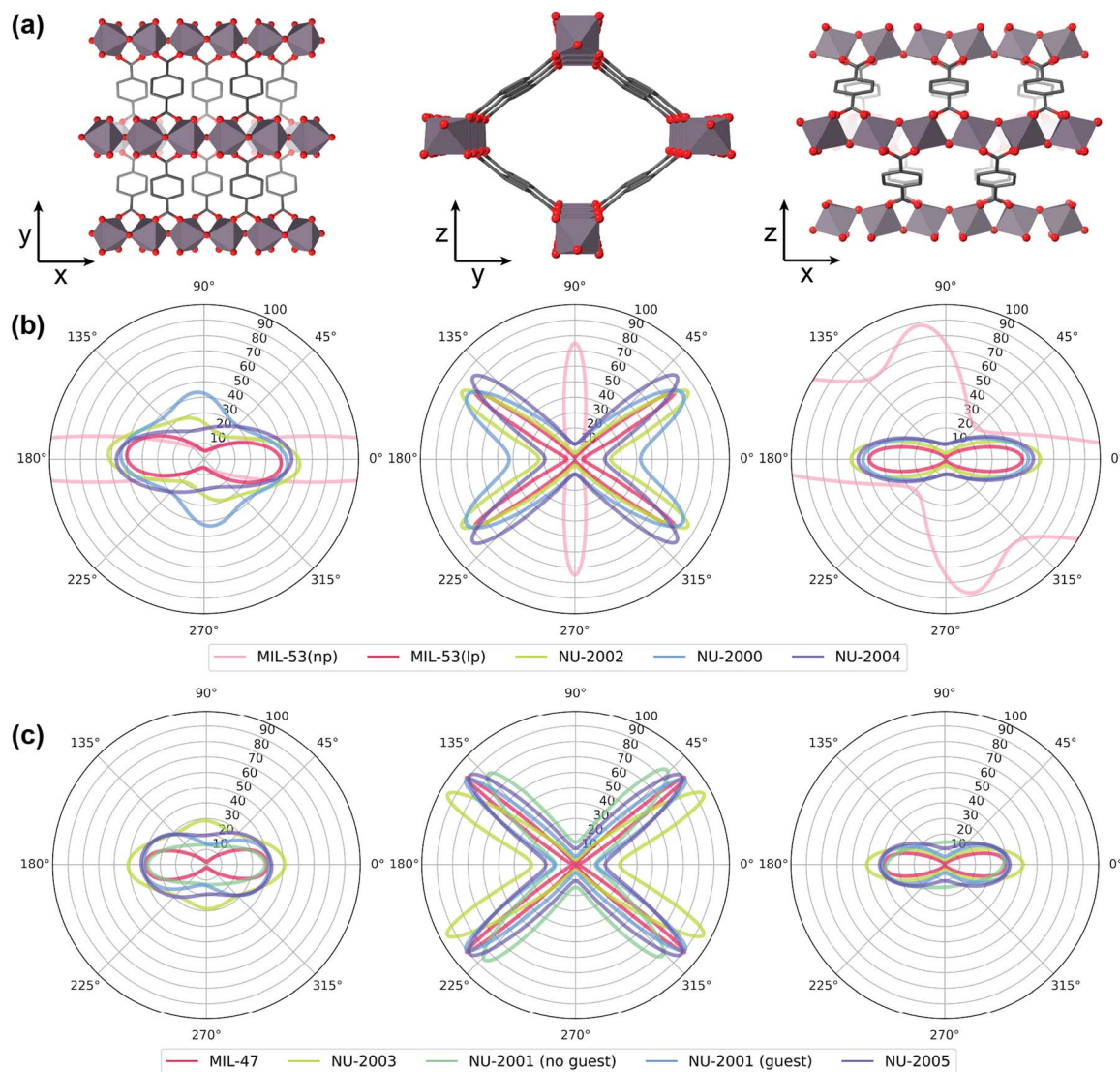


Fig. 3 (a) Projections of the xy -, yz -, and xz -planes in MIL-53 and the corresponding Young's modulus profiles for the (b) aluminum and (c) vanadium analogues.

NU-2000, and NU-2004 demonstrate higher values of 3.9, 9.8, and 9.6 GPa, respectively. Similarly, the Young's modulus of MIL-53(Al) in the y -direction is 5.3, while the 3D linker

analogues of increasing bulkiness exhibit values of 23.3, 42.6, and 19.4 GPa (Fig. 3b and Table 1). We observed similar trends in the vanadium structures (Fig. 3c and Table 1). In all open

Table 1 Young's moduli values calculated from elastic tensors

MOF		Maximum (GPa)	y -direction (GPa)	z -direction (GPa)
Al nodes	MIL-53 (np)	75.1	5.8	75.1
	MIL-53 (lp)	78.0	5.3	1.2
	NU-2002	85.1	23.3	3.9
	NU-2000	81.2	42.6	9.8
	NU-2004	85.0	19.4	9.6
V nodes	MIL-47(V)	90.8	2.1	0.9
	NU-2003	95.0	28.6	3.5
	NU-2001 (no guest)	90.1	13.7	5.5
	NU-2001 (guest)	85.5	13.0	14.8
	NU-2005	89.9	19.2	10.7

pore cases, the maximum values of Young's moduli are in the direction of the linkers and lie between 75 and 95 GPa. Interestingly, despite the aliphatic nature of the BPDCA and BODCA linkers, there is no significant decrease in compressibility in the direction of the linker components.

Overall, we ascribe the elastic behavior of our 3DL-based structures to the wine-rack motif and their "open" pores. Our calculations show that increasing linker dimensionality from 2D to 3D does rigidify MOFs in the *sra* topology, both globally (as depicted in the energy-volume diagrams in Fig. 2c and d) and locally. Next, we conducted compressibility experiments on selected 3D linker-based MOFs to understand their behavior in practical conditions and compare our computational results with our experimental observations.

Role of structural flexibility in compressibility experiments

To probe the experimental performance of 3D linker-based MOFs under pressure, we conducted *in situ* variable pressure X-ray diffraction on four representative 3D linker-based structures—NU-2000 ([Al(OH)BODCA]), NU-2002 ([Al(OH)BPDCA]), NU-2003 ([V(O)BPDCA]), and NU-2005 ([V(O)*p*C]). Note that we are reporting the structure of NU-2003 for the first time here, and its synthesis procedure and crystallographic information are detailed in the ESI (Section 1.1.1, Table S2, and Fig. S8†). These experiments were performed at the 17-BM-B beamline at the Advanced Photon Source at Argonne National Laboratory using a membrane-driven diamond anvil cell (DAC). The DAC was packed with a mixture of MOF, CaF₂ (internal pressure standard), and

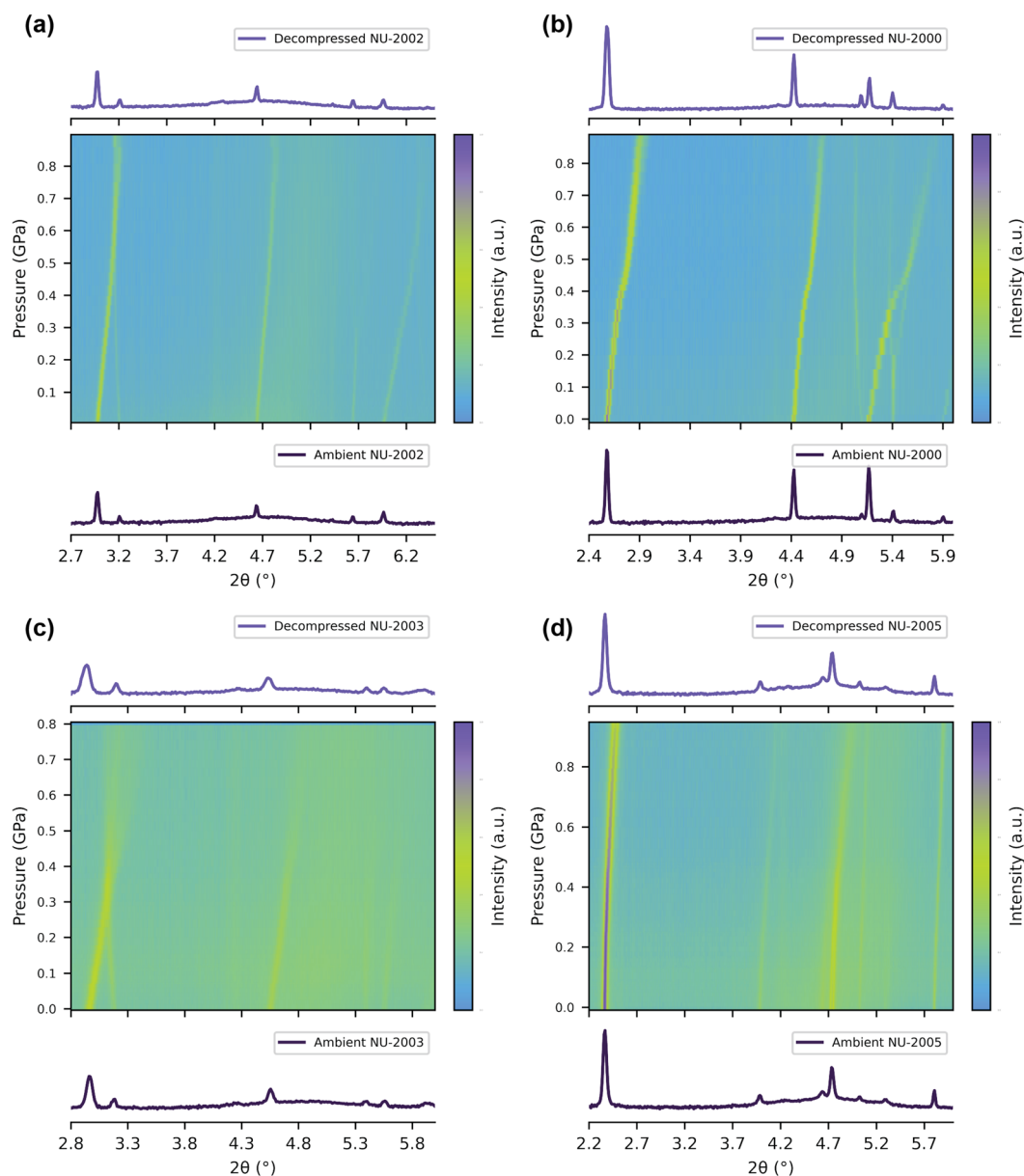


Fig. 4 Ambient (room temperature and 0 GPa) powder X-ray diffraction (PXRD) patterns collected prior to compression experiments (bottom), PXRD patterns collected during compression experiments up to about 1 GPa (middle), and PXRD patterns collected after decompression of the diamond anvil cell (top) for (a) NU-2002, (b) NU-2000, (c) NU-2003, and (d) NU-2005.

Fluorinert FC-70 (non-penetrating pressure transmitting medium), as detailed in our previously published procedures.^{34–36} During the experiments, each material was gradually compressed from 0 to 1 GPa, while collecting diffraction data from monochromatic X-rays ($\lambda = 0.452 \text{ \AA}$). This setup allows us to probe the material's behavior under mechanical pressure that is uniform in all directions, rather than uniaxially as described in the previous section.

Previously, Yot *et al.* performed similar experiments using MIL-47(V), showing that the 2D linker-based structure contracts from its large pore phase to its closed pore phase at a pressure of 0.34 GPa.³³ This phase change was evidenced by a sudden change in the diffraction pattern. However, when compressing the 3D linker-based structures, we did not observe obvious phase changes in the X-ray diffraction patterns (Fig. 4), further supporting that installing 3D linkers prevents global phase transitions to closed pore phases, as we predicted from their energy–volume diagrams (Fig. 2c and d). Instead, Fig. 4 shows continuous shifts of the peaks to higher angles, signaling uniform contraction of their unit cells upon pressurization, consistent with elastic (reversible) compression.

NU-2002, NU-2000, and NU-2005 all retained crystallinity up to approximately 1 GPa, while NU-2003 amorphized around 0.5 GPa. After the pressure campaigns were complete, we decompressed the cell and collected additional PXRD data. After decompression of the cell, all structures – even NU-2003 – showed crystallinity and peak positions that corresponded with their original positions at ambient conditions (Fig. 4), reaffirming that the compression process occurred in the elastic regime. In addition to this qualitative analysis of the PXRD data, we calculated each material's bulk modulus, *i.e.* the material's resistance to volumetric change when it is subjected to uniform pressure from all directions (Fig. S1†). We derived the bulk moduli by fitting the unit cell volume and pressure data to the 2nd order Birch–Murnaghan equation of state in the initial linear region (Fig. S15†).³⁷

Similar to our analysis of Young's moduli, which only describes behavior in the elastic regime, we use the bulk modulus as a metric of local flexibility (where lower values signify

increased local flexibility). The unit cell volume and system pressure were derived by sequentially fitting the MOF peaks and the CaF_2 peaks, respectively. We calculated values of 7.0 ± 0.1 and 6.4 ± 0.2 GPa for the aluminum analogues, NU-2002 and NU-2000, respectively. For the vanadium analogues, we calculated values of 5.2 ± 0.1 GPa and 25.0 ± 0.3 GPa for NU-2003 and NU-2005, respectively. Notably, the high bulk modulus for NU-2005 highlights the stability imparted by the 3D, aromatic *pC* ligand, which also imparts significant thermal stability as described in our previous work.¹² Although the bulk moduli values of the other 3D linker-based structures are lower in comparison, the ability of each of these structures to recover their crystallinity and return to their original lattice parameters upon decompression of the cell underscores the impact that local flexibility can have on the mechanical stability of MOFs (Fig. 4), a metric that conventional values of mechanical stability cannot necessarily quantify, especially for materials with high anisotropy.

To compare the effects of linker dimensionality (2D vs. 3D) and linker bulkiness ($\text{BDC} < \text{BPDCA} < \text{BODCA} < pC$) on the bulk modulus, we also derived the bulk moduli for all the MOFs studied in this work by fitting the energy–volume profiles (from Fig. 2) using the Vinet equation of state (Fig. S11–S14†). Because of the potential overestimation of dispersion forces by the empirical dispersion correction and the 0 K approximation in our DFT calculations,³⁸ the computationally derived bulk modulus values are generally underestimated when compared to the experimentally derived values from room temperature (Table S4†). However, this analysis still allows us to probe the correlation between linker bulkiness and bulk modulus on the complete set of analogous structures by assessing qualitative trends (Fig. 5).

In the aluminum analogues, we see that increasing linker dimensionality and bulkiness has a positive correlation on the computationally derived bulk modulus, with increasing values of 1.3, 1.8, 3.0, and 8.0 GPa for the BDC (large pore), BPDCA, BODCA, and *pC* ligand, respectively (Fig. 5a). This trend demonstrates that increasing linker bulkiness has a positive correlation with overall rigidity in the elastic regime, improving its resistance to deformation under elastic compression

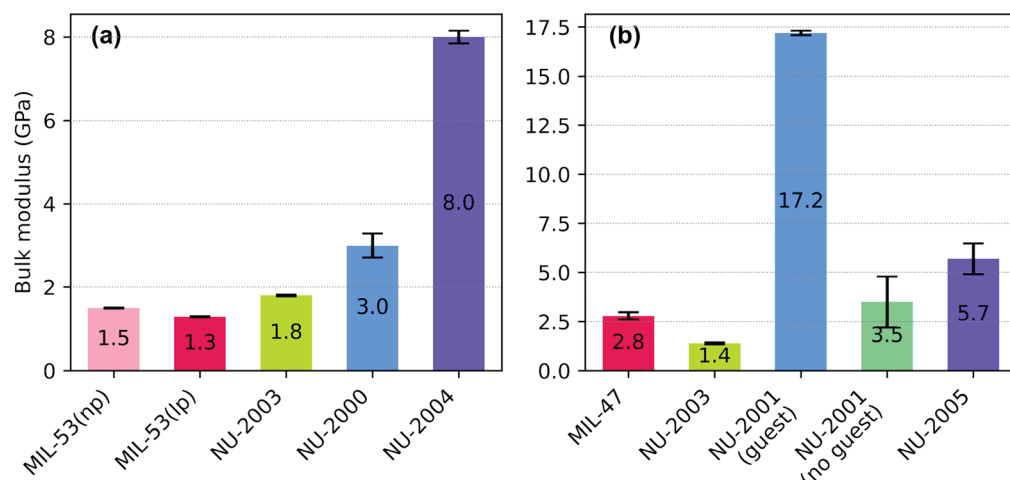


Fig. 5 Bulk modulus values for (a) aluminum structures and (b) vanadium structures derived from fitting DFT energy–volume diagrams with the Vinet equation of state.



conditions. Further, our bulk moduli results reinforce our conclusions from calculating the Young's moduli that increasing linker dimensionality from 2D to 3D instills local rigidity. However, because the vanadium system has more complexities, it does not necessarily follow this trend (Fig. 5b). Specifically, additional linkers in the pores of NU-2001 (guest) further stabilize its structure (Fig. S2a†), resulting in a high bulk modulus value of 17.2 GPa. To address this discrepancy, we also calculated the bulk modulus for the hypothetical structure of NU-2001 (no guest), as it does not contain additional stabilizing linker in its pores. When comparing the bulk moduli values using this structure, we see an increasing trend in bulk modulus from NU-2003 to NU-2001 (no guest) to NU-2005, which is consistent with our calculations for the aluminum-based analogues. Excluding the bulk modulus of NU-2001 (guest), NU-2005 has the highest bulk modulus value for the vanadium system due to the incorporation of the *pC* ligand, which is consistent with our experimental results.

Implications of global and local flexibility on adsorption

To demonstrate the implications of each type of flexibility on gas adsorption in MOFs (and ultimately their effects on practical separation applications), we simulated argon adsorption at

87 K using grand canonical Monte Carlo simulations in several structures derived from our DFT geometry optimizations (see ESI Section 2.3 for details†). We performed these simulations using the gRASP code, an open source code that uses graphical processing units for performance-enhanced Monte Carlo simulations.³⁹ First, we compared argon uptake in the narrow pore and large pore structures of MIL-53(Al) to highlight the impact of global flexibility on gas adsorption uptake. In the narrow pore structure, we observed no uptake of argon as the pore size is too small for any adsorption. However, the large pore structure shows significant uptake of 18 mol Ar per kg (Fig. 6b), highlighting the significant impact that breathing behavior can have on a material's adsorption properties.

To emulate the effects of local flexibility on adsorption, we simulated argon adsorption on 3 different fixed-volume optimized structures of NU-2002, with increasing unit cell volumes (1104, 1126, and 1151 Å³). We selected these structures because they sit near the bottom of the energy well in the energy–volume diagram for NU-2002 (see Fig. 6a) and could theoretically be accessed *via* changes in temperature, pressure, *etc.* As expected, we see slight increases in argon adsorption between 1104 and 1151 Å³ (Fig. 6c) at saturation and a shift in uptake to higher values in the low-pressure region, underscoring that local flexibility has implications on the adsorption properties of MOFs that should be

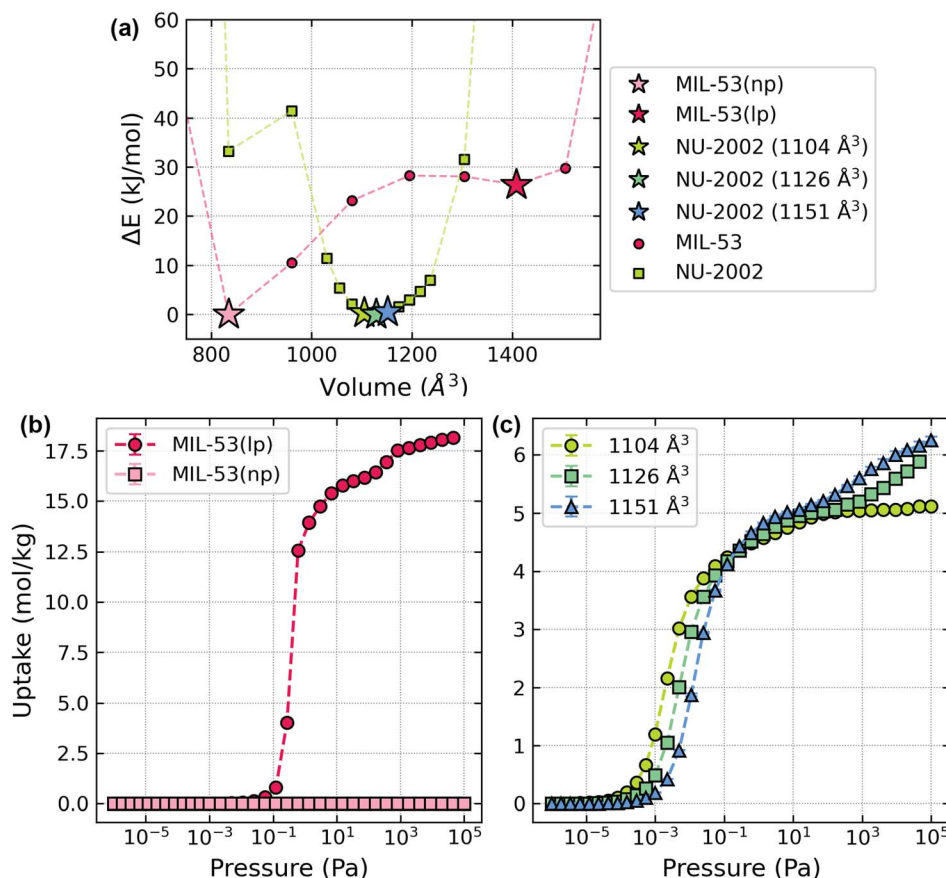


Fig. 6 (a) Energy–volume diagrams for MIL-53(Al) and NU-2002 with stars emphasizing the selected structures and volumes used in our adsorption simulations. (b) Argon adsorption in the narrow pore (light pink) and the large pore (dark pink) forms of MIL-53 on log scale to demonstrate the impact of global flexibility on adsorption. (c) Argon adsorption in structures of NU-2002 with volumes of 1104, 1126, and 1151 Å³ to emphasize the impact of local flexibility on adsorption. All adsorption data is from grand canonical Monte Carlo (GCMC) simulations at 87 K.

considered for separations applications. However, the differences in adsorption between the structures demonstrating local flexibility are significantly lower than the differences observed with the MIL-53(Al) structures that demonstrate global flexibility.

Conclusions

Using a combination of computational methods and compressibility experiments, we fully characterized the nature of structural flexibility (local or global) and its extent in 3D linker-based MOFs. These findings enabled our understanding of the effects of flexibility on sub-angstrom pore control and mechanical stability in these systems. From DFT geometry optimizations, we produced energy–volume diagrams, which showed that increasing linker dimensionality from 2D to 3D reduces the number of possible phases from 2 to 1 in these systems, eliminating global flexibility and associated structural phase transitions as a result. We also leveraged conventional mechanical properties, which describe material behavior in the elastic regime, to quantify local flexibility. Our results show that the 3D linker-based structures mimic the spatially dependent Young's moduli profiles of the open pore structures of MIL-53(Al) and MIL-47(V), with higher values of Young's moduli in the key *y*- and *z*-directions in comparison with the 2D linker analogues. These results indicate that 3D linkers reduce flexibility in the *sra* topology both locally and globally. To understand these findings in practical conditions, we conducted compressibility experiments using *in situ* variable pressure powder X-ray diffraction. These experiments reveal that, upon application of mechanical pressure, 3D linker-based MOFs show continuous contraction of their unit cell, rather than a sudden contraction to a closed pore phase, further highlighting the elimination of global flexibility. Upon decompression of the cell, the peaks revert to their original positions, demonstrating mechanical stability imparted by the local flexibility of these materials. Finally, we used GCMC simulations of argon adsorption to demonstrate the implications of flexibility on the adsorption properties of MOFs. Overall, we show a positive correlation between sub-angstrom pore control and increased mechanical stability.

Developing a complete understanding of the structural flexibility in these systems, provides a compelling rationale for the classification of flexibility into two categories, based on the energetics driving the structural changes. Appropriately categorizing and comparing flexibility in porous materials is important for understanding their mechanical stability and gas adsorption properties—factors that are crucial for potential industrialization of these materials. Our work provides a framework for quantifying each type of flexibility and understanding their implications in practical conditions. Our analysis of local *versus* global flexibility demonstrates that all MOFs can display some flexibility, but further analysis is critical to understand the type and extent.

Data availability

The data supporting this article have been included as part of the ESI.† Crystallographic data for NU-2003 has been deposited at the CCDC 2347333.

Author contributions

C. S. S. wrote the manuscript. C. S. S. and F. F. performed all DFT calculations and GCMC simulations. C. S. S. and K. B. I. synthesized and characterized the materials used in the experimental portion of this study. C. S. S., M. L. B., K. M. F., M. A. G., and F. A. S. contributed to the collection of diffraction data at the Advanced Photon Source at Argonne National Laboratory. H. X. collected the single crystal X-ray diffraction data and solved the structure of NU-2003. O. K. F. and R. Q. S. supervised the project. All authors contributed to editing the manuscript.

Conflicts of interest

O. K. F. and R. Q. S. have a financial interest in NuMat Technologies, a startup company that is seeking to commercialize MOFs. All other authors declare no competing interests.

Acknowledgements

C. S. S. would like to thank Dr Wenqian Xu and Dr Andrey Yakovenko from the Advanced Photon Source at Argonne National Laboratory for their kind help in setting up high pressure experiments. R. Q. S. gratefully acknowledges support from the Separation Science program of the U.S. Department of Energy (DE-FG02-08ER15967). O. K. F. gratefully acknowledges support from the Defense Threat Reduction Agency (HDTRA1-19-1-0007). We gratefully acknowledge the computational resources provided by the National Energy Research Scientific Computing Center (NERSC), a DOE Office of Science User Facility supported by the Office of Science of the U.S. Department of Energy under contract no. DE-AC02-05CH11231. Additionally, we acknowledge the Polish high-performance computing infrastructure PLGrid (HPC Center: ACK Cyfronet AGH) for providing computer facilities and support within computational grant no. PLG/2024/016965. This work made use of the IMSERC (Integrated Molecular Structure Education and Research Center) X-ray facility at Northwestern University, which has received support from the Soft and Hybrid Nanotechnology Experimental (SHyNE) Resource (NSF ECCS-2025633), and Northwestern University. C. S. S., M. L. B., M. A. G., and F. A. S. gratefully acknowledge support from the Ryan Fellowship and the International Institute of Nanotechnology at Northwestern University. F. F. is supported by the Polish National Agency for Academic Exchange (decision no. BPN/BEK/2021/1/00184/DEC/). K. M. F. is supported by the National Science Foundation Graduate Research Fellowship (NSF GRFP) under Grant No. DGE-1842165. M. L. B. would like to thank Vinayak P. Dravid for his advising support.

Notes and references

- 1 J. R. Li, R. J. Kuppler and H. C. Zhou, Selective gas adsorption and separation in metal–organic frameworks, *Chem. Soc. Rev.*, 2009, **38**, 1477–1504.
- 2 J. R. Li, J. Sculley and H. C. Zhou, Metal–Organic Frameworks for Separations, *Chem. Rev.*, 2012, **112**, 869–932.



- 3 M. S. Denny, J. C. Moreton, L. Benz and S. M. Cohen, Metal-organic frameworks for membrane-based separations, *Nat. Rev. Mater.*, 2016, **1**, 16078.
- 4 X. Zhao, Y. X. Wang, D. S. Li, X. H. Bu and P. Y. Feng, Metal-Organic Frameworks for Separation, *Adv. Mater.*, 2018, **30**, 1705189.
- 5 H. Furukawa, K. E. Cordova, M. O'Keeffe and O. M. Yaghi, The chemistry and applications of metal-organic frameworks, *Science*, 2013, **341**, 1230444.
- 6 A. Schneemann, V. Bon, I. Schwedler, I. Senkovska, S. Kaskel and R. A. Fischer, Flexible metal-organic frameworks, *Chem. Soc. Rev.*, 2014, **43**, 6062–6096.
- 7 R. B. Lin, L. B. Li, H. L. Zhou, H. Wu, C. H. He, S. Li, R. Krishna, J. P. Li, W. Zhou and B. L. Chen, Molecular sieving of ethylene from ethane using a rigid metal-organic framework, *Nat. Mater.*, 2018, **17**, 1128.
- 8 A. Cadiau, K. Adil, P. M. Bhatt, Y. Belmabkhout and M. Eddaoudi, A metal-organic framework-based splitter for separating propylene from propane, *Science*, 2016, **353**, 137–140.
- 9 R. B. Lin, S. C. Xiang, W. Zhou and B. L. Chen, Microporous Metal-Organic Framework Materials for Gas Separation, *Chem*, 2020, **6**, 337–363.
- 10 J. Zhou, T. Ke, Y. Song, H. Cai, Z. Wang, L. Chen, Q. Xu, Z. Zhang, Z. Bao, Q. Ren and Q. Yang, Highly Efficient Separation of C8 Aromatic Isomers by Rationally Designed Nonaromatic Metal-Organic Frameworks, *J. Am. Chem. Soc.*, 2022, **144**, 21417–21424.
- 11 C. S. Smoljan, Z. Li, H. Xie, C. J. Setter, K. B. Idrees, F. A. Son, F. Formalik, S. Shafaie, T. Islamoglu, L. K. Macreadie, R. Q. Snurr and O. K. Farha, Engineering Metal-Organic Frameworks for Selective Separation of Hexane Isomers Using 3-Dimensional Linkers, *J. Am. Chem. Soc.*, 2023, **145**, 6434–6441.
- 12 K. B. Idrees, K. O. Kirlikovali, C. Setter, H. Xie, H. Brand, B. Lal, F. Sha, C. S. Smoljan, X. Wang, T. Islamoglu, L. K. Macreadie and O. K. Farha, Robust Carborane-Based Metal-Organic Frameworks for Hexane Separation, *J. Am. Chem. Soc.*, 2023, **145**, 23433–23441.
- 13 K. B. Idrees, Z. Li, H. M. Xie, K. O. Kirlikovali, M. Kazem-Rostami, X. J. Wang, X. J. Wang, T. Y. Tai, T. Islamoglu, J. F. Stoddart, R. Q. Snurr and O. K. Farha, Separation of Aromatic Hydrocarbons in Porous Materials, *J. Am. Chem. Soc.*, 2022, **144**, 12212–12218.
- 14 B. Lal, K. B. Idrees, H. Xie, C. S. Smoljan, S. Shafaie, T. Islamoglu and O. K. Farha, Pore Aperture Control Toward Size-Exclusion-Based Hydrocarbon Separations, *Angew Chem. Int. Ed. Engl.*, 2023, e202219053, DOI: [10.1002/anie.202219053](https://doi.org/10.1002/anie.202219053).
- 15 C. S. Smoljan, F. R. Sha, P. Campitelli, H. M. Xie, M. A. Eddaoudi, M. R. Mian, C. Di Nicola, K. O. Kirlikovali, R. Q. Snurr and O. K. Farha, Constraining Flexibility in the MIL-88 Topology through Integration of 3-Dimensional Linkers, *Cryst. Growth Des.*, 2024, **24**, 3941–3948.
- 16 J. Zhou, K. Wen, T. Ke, J. Li, Y. Jin, J. Li, Z. Zhang, Z. Bao, Q. Ren and Q. Yang, Nonlinear 3D Ligand-Based Metal-Organic Framework for Thermodynamic-Kinetic Synergistic Splitting of Mono-/Dibranched Hexane Isomers, *J. Am. Chem. Soc.*, 2024, **146**, 16838–16847.
- 17 L. K. Macreadie, K. B. Idrees, C. S. Smoljan and O. K. Farha, Expanding Linker Dimensionality in Metal-Organic Frameworks for sub-Angstrom Pore Control for Separation Applications, *Angew Chem. Int. Ed. Engl.*, 2023, e202304094, DOI: [10.1002/anie.202304094](https://doi.org/10.1002/anie.202304094).
- 18 D. Fairen-Jimenez, R. Galvelis, A. Torrisi, A. D. Gellan, M. T. Wharmby, P. A. Wright, C. Mellot-Draznieks and T. Duren, Flexibility and swing effect on the adsorption of energy-related gases on ZIF-8: combined experimental and simulation study, *Dalton Trans.*, 2012, **41**, 10752–10762.
- 19 D. Fairen-Jimenez, S. A. Moggach, M. T. Wharmby, P. A. Wright, S. Parsons and T. Duren, Opening the Gate: Framework Flexibility in ZIF-8 Explored by Experiments and Simulations, *J. Am. Chem. Soc.*, 2011, **133**, 8900–8902.
- 20 F. Formalik, B. Mazur, M. Fischer, L. Firlej and B. Kuchta, Phonons and Adsorption-Induced Deformations in ZIFs: Is It Really a Gate Opening?, *J. Phys. Chem. C*, 2021, **125**, 7999–8005.
- 21 J. Perego, C. X. Bezuidenhout, S. Bracco, S. Piva, G. Prando, C. Aloisi, P. Carretta, J. Kaleta, T. P. Le, P. Sozzani, A. Daolio and A. Comotti, Benchmark Dynamics of Dipolar Molecular Rotors in Fluorinated Metal-Organic Frameworks, *Angew. Chem., Int. Ed.*, 2023, **62**, e202215893.
- 22 C. S. Smoljan, R. Q. Snurr and O. K. Farha, 3-dimensional linker-based metal-organic frameworks for sub-angstrom control and enhanced thermal stability, *J. Mater. Res.*, 2024, 1047–1056, DOI: [10.1557/s43578-024-01309-5](https://doi.org/10.1557/s43578-024-01309-5).
- 23 Y. Liu, J. H. Her, A. Dailly, A. J. Ramirez-Cuesta, D. A. Neumann and C. M. Brown, Reversible structural transition in MIL-53 with large temperature hysteresis, *J. Am. Chem. Soc.*, 2008, **130**, 11813–11818.
- 24 T. Loiseau, C. Serre, C. Huguenard, G. Fink, F. Taulelle, M. Henry, T. Bataille and G. Férey, A rationale for the large breathing of the porous aluminum terephthalate (MIL-53) upon hydration, *Chemistry*, 2004, **10**, 1373–1382.
- 25 A. E. J. Hoffman, J. Wieme, S. M. J. Rogge, L. Vanduyfhuys and V. Van Speybroeck, The impact of lattice vibrations on the macroscopic breathing behavior of MIL-53(Al), *Z. Kristallogr. - Cryst. Mater.*, 2019, **234**, 529–545.
- 26 F. Millange, C. Serre and G. Férey, Synthesis, structure determination and properties of MIL-53as and MIL-53ht: the first Cr hybrid inorganic-organic microporous solids: Cr(OH)•{OC-CH-CO}•{HOC-CH-COH}, *Chem. Commun.*, 2002, 822–823, DOI: [10.1039/b201381a](https://doi.org/10.1039/b201381a).
- 27 K. Barthelet, J. Marrot, D. Riou and G. Férey, A breathing hybrid organic-inorganic solid with very large pores and high magnetic characteristics, *Angew. Chem., Int. Ed.*, 2002, **41**, 281.
- 28 J. P. S. Mowat, V. R. Seymour, J. M. Griffin, S. P. Thompson, A. M. Z. Slawin, D. Fairen-Jimenez, T. Duren, S. E. Ashbrook and P. A. Wright, A novel structural form of MIL-53 observed for the scandium analogue and its response to temperature variation and CO₂ adsorption, *Dalton Trans.*, 2012, **41**, 3937–3941.



- 29 F. Formalik, A. V. Neimark, J. Rogacka, L. Firlej and B. Kuchta, Pore opening and breathing transitions in metal-organic frameworks: Coupling adsorption and deformation, *J. Colloid Interface Sci.*, 2020, **578**, 77–88.
- 30 R. Gaillac, P. Pullumbi and F. X. Coudert, ELATE: an open-source online application for analysis and visualization of elastic tensors, *J. Phys.:Condens. Matter*, 2016, **28**, 275201.
- 31 A. U. Ortiz, A. Boutin, A. H. Fuchs and F. X. Coudert, Metal-organic frameworks with wine-rack motif: what determines their flexibility and elastic properties?, *J. Chem. Phys.*, 2013, **138**, 174703.
- 32 A. U. Ortiz, A. Boutin, A. H. Fuchs and F. X. Coudert, Anisotropic elastic properties of flexible metal-organic frameworks: how soft are soft porous crystals?, *Phys. Rev. Lett.*, 2012, **109**, 195502.
- 33 P. G. Yot, Q. T. Ma, J. Haines, Q. Y. Yang, A. Ghoufi, T. Devic, C. Serre, V. Dmitriev, G. Férey, C. L. Zhong and G. Maurin, Large breathing of the MOF MIL-47(V) under mechanical pressure: a joint experimental-modelling exploration, *Chem. Sci.*, 2012, **3**, 1100–1104.
- 34 L. R. Redfern, L. Robison, M. C. Wasson, S. Goswami, J. F. Lyu, T. Islamoglu, K. W. Chapman and O. K. Farha, Porosity Dependence of Compression and Lattice Rigidity in Metal-Organic Framework Series, *J. Am. Chem. Soc.*, 2019, **141**, 4365–4371.
- 35 L. Robison, X. Y. Gong, A. M. Evans, F. A. Son, X. J. Wang, L. R. Redfern, M. C. Wasson, Z. H. Syed, Z. J. Chen, K. B. Idrees, T. Islamoglu, M. Delferro, W. R. Dichtel, F. X. Coudert, N. C. Gianneschi and O. K. Farha, Transient Catenation in a Zirconium-Based Metal-Organic Framework and Its Effect on Mechanical Stability and Sorption Properties, *J. Am. Chem. Soc.*, 2021, **143**, 1503–1512.
- 36 F. A. Son, K. M. Fahy, M. A. Gaidimas, C. S. Smoljan, M. C. Wasson and O. K. Farha, Investigating the mechanical stability of flexible metal-organic frameworks, *Commun. Chem.*, 2023, **6**, 185.
- 37 F. Birch, Finite Elastic Strain of Cubic Crystals, *Phys. Rev.*, 1947, **71**, 809–824.
- 38 J. Wieme, K. Lejaeghere, G. Kresse and V. Van Speybroeck, Tuning the balance between dispersion and entropy to design temperature-responsive flexible metal-organic frameworks, *Nat. Commun.*, 2018, **9**, 4899.
- 39 Z. Li, K. H. Shi, D. Dubbeldam, M. Dewing, C. Knight, A. Vázquez-Mayagoitia and R. Q. Snurr, Efficient Implementation of Monte Carlo Algorithms on Graphical Processing Units for Simulation of Adsorption in Porous Materials, *J. Chem. Theory Comput.*, 2024, **20**, 10649–10666.

